Ancestral reconstruction of polyethylene terephthalate degrading cutinases reveals a rugged and unexplored sequence-fitness landscape

Vanessa Vongsouthi[1,2#], Rosemary Georgelin[1#], Dana Matthews[1,2#], Jake Saunders[1], Brendon M. Lee[1], Jennifer Ton[2], Adam M. Damry[1], Rebecca L. Frkic[1,3], Matthew A. Spence[1,2*], Colin J. Jackson[1,2,3,4*]

1 Research School of Chemistry, Australian National University, Canberra, ACT 2601, Australia

2 Samsara Eco, Sydney, NSW 2065, Australia

3 ARC Centre of Excellence for Innovations in Peptide & Protein Science, Research School of Chemistry, Australian National University, Canberra, ACT 2601, Australia

4 ARC Centre of Excellence for Innovations in Synthetic Biology, Research School of Chemistry, Australian National University, Canberra, ACT 2601, Australia

[#] These authors contributed equally to this work.

*To whom correspondence should be addressed: colin.jackson@anu.edu.au

The enzymatic degradation of polyethylene terephthalate (PET) is a promising method of advanced plastic recycling. Traditional protein engineering methods often fall short in exploring protein sequence space for optimal enzymes due to structural and rational design limitations. Our study addresses this by using multiplexed ancestral sequence reconstruction (mASR) to explore the evolutionary sequence space of PET-degrading cutinases. With a dataset of 397 cutinase sequences, we created a diverse library of ancestral sequences. Experimental characterization of 48 ancestral sequences revealed a wide range of PETase activities, highlighting the value of mASR in uncovering functional variants when compared to traditional ASR. Our results showed that PETase activity in cutinases evolved through diverse pathways involving distal mutations to the active site, and is readily accessible within this family. Additionally, our analysis of the PETase fitness landscape using one-hot encoding (OHE) and local ancestral sequence embedding (LASE) highlighted the effectiveness of LASE in capturing sequence features relevant to activity. This work emphasizes the utility of mASR as a protein engineering tool for identifying enhanced PET-degrading enzymes, and the advantages of the LASE embedding scheme in mapping the PETase fitness landscape.

Introduction

Over 350 million tonnes of plastic are produced annually, with the majority being derived from petrochemicals[1]. However, the current global recycling rate of plastics is estimated to be less than 10%, partially due to the technological constraints of mechanical (melt-extrusion) recycling[2]. There is a pressing need to develop advanced and scalable recycling methods that will enable the transition towards a circular plastic economy. In the last decade, enzymatic depolymerization of plastics has emerged as one such advanced recycling method[3]. The enzymatic degradation of polyethylene terephthalate (PET), a versatile thermoplastic commonly found in food and beverage packaging, and polyester textiles has received particular interest[3].

PET-degrading enzymes that have been characterized to date, including those classified as cutinases[4–6] (EC 3.1.1.74), lipases[7] (EC 3.1.1.3), and carboxylesterases[8] (EC 3.1.1.1), belong to the esterase subclass (EC 3.1) and are characterized by a catalytic triad (Ser-His-Asp) typical of the α/β hydrolase fold superfamily. Cutinases have garnered significant interest due to their ability to hydrolyse both aromatic and aliphatic polyesters[9]. Cutinases of bacterial[5,9,10], fungal[7], and metagenomic[11–13] origins have been studied for their PETase activity, including Thc_Cut1 and Thc_Cut from *Thermobifida cellulosilytica*[5], TfCut2 from *Thermobifida fusca*[5], HiC from *Humicola insolens*[14], FsC from *Fusarium solani pisi*[15], and LCC from leaf-branch compost metagenome[16]. However, extant cutinases are often unsuitable for direct use in industrial processes, necessitating optimisation to improve properties such as catalytic efficiency[17], stability under harsh conditions[18,19], and to alleviate product inhibition[20]. For example, active site optimisation through rational design[6,10,21] and evolutionarily-guided engineering[20] has yielded significant improvements in PET hydrolysis across various cutinase backgrounds. While structure-guided protein engineering has been effective in improving the efficiency of extant PETases, it has provided little insight on the mechanisms by which PETase activity emerges or has been optimized by evolution.

Ancestral sequence reconstruction (ASR), which utilizes a phylogenetic tree and a statistical model of evolution to infer the sequences of extinct, ancestral proteins, can provide critical insights into molecular evolution and functional diversification within protein families[22]. ASR has been useful in studying sequence-function relationships over protein families[23,24]; such insight can shed light on the topologies of fitness landscapes that dictate the adaptive potential of proteins[25]. For example, ASR can give insight into the ruggedness (i.e. complexity) of a fitness landscape over large spans of evolutionarily accessible sequence space to reveal

fitness peaks that are inaccessible through stepwise mutational approaches[24]. In addition to this, ASR is also frequently used to engineer enzymes with enhanced industrial properties[22,26–28], making it a valuable tool in both protein engineering and understanding the mechanisms of molecular evolution.

More recently, protein representation learning has become a widely used method in protein engineering and evolutionary inference[29,30]. Protein language models (PLM), which are deep neural networks trained to predict the identities of masked residues in a corpus of protein sequences[29–32], can map information sparse and high dimensional protein sequences to fixed-length vector representations. These vector representations capture the evolutionary and biophysical features of protein sequences in the representation model's latent embedding space[29,30]. Indeed, PLMs have been used to learn the structure of fitness landscapes[33–35], and can learn evolutionary features when trained with ancestrally reconstructed sequence data[36].

In this study, we applied ASR to explore the evolutionarily accessible sequence space of PET-degrading cutinases. Using a dataset of 397 extant cutinase sequences with significant homology to known cutinases with PETase activity, we adopted a multiplexed ASR (mASR) approach to generate a diverse library of ancestral cutinase sequences. Through experimental characterization of 48 ancestral cutinases, we identified a broad range of PETase activities, including between equivalent nodes on distinct yet statistically indifferent phylogenetic topologies. Such findings highlight the importance of sampling diverse phylogenetic backgrounds to uncover functional ancestral variants. Furthermore, our study analyzed the topology of the PETase fitness landscape through two sequence embedding schemes: one-hot encoding (OHE) and the more recently described local ancestral sequence embedding (LASE)[36]. We found that LASE was more effective in capturing cutinase sequence features pertinent to PETase activity, demonstrating a clear pattern of iterative improvement in PETase functionality throughout the sequence exploration phases of our study. This comprehensive approach not only highlights the utility of mASR in uncovering novel PETase variants but also emphasizes the role of advanced embedding techniques in mapping PETase fitness landscapes.

Results

Multiplexed ASR yields functional PETases from diverse phylogenetic backgrounds.

We used ASR to explore the PETase functional sequence space of the cutinase family. To maximize diversity in the local sequence space around known PETases, such as *Tf*Cut2 and LCC, we employed the recently described multiplexed ASR (mASR)[36]. In brief, mASR samples multiple statistically indifferent phylogenetic backgrounds from which to reconstruct ancestral sequences from. This produces diverse libraries of ancestral proteins that span functional sequence space over a distribution of realistic phylogenies. To achieve this, we performed 20 replicates of maximum likelihood (ML) phylogenetic inference and ASR on a single dataset of 397 extant cutinases with significant homology to *Tf*cut2 and LCC (E-value <= 1E-5). Consistent with previous phylogenetic studies[37], PET hydrolytic cutinases were resolved as a polyphyletic group of two monophyletic lineages: the *Thermobifida sp*. PETases, which include *Tf*cut2, *T. cellulosytica* cutinase and *T. alba* esterase 1 and the LCC-like PETases that include LCC and BhrPETase. This topology was resolved consistently over all 20 phylogenetic priors used for mASR (**Figure 1A**). The placement of the PETase clades were supported by high ultra-fast bootstrap approximations[38] (>= 0.95) and the ancestral nodes separating these groups were reconstructed in CodeML from the PAML[39] suite with relatively high mean posterior probability (>0.9; based on ASR statistical benchmarking studies[40]). The resulting ancestral sequence library comprised approximately 1600 unique sequences that encompassed the evolutionarily accessible sequence space of the bacterial cutinase family.

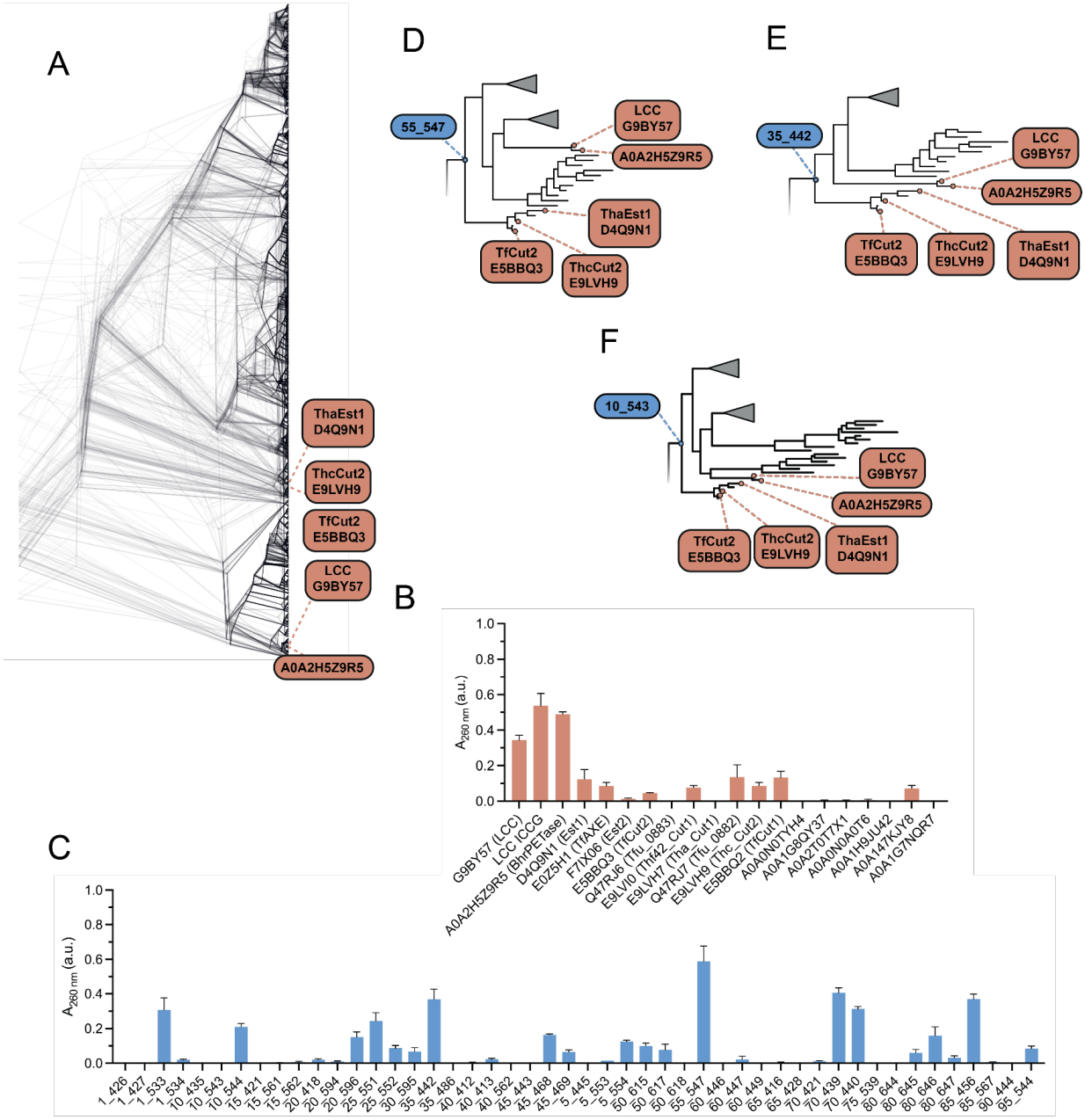

Figure 1. Ancestral sequence reconstruction and characterization of ancestral cutinases. (**A**) 20 replicates of phylogenetic reconstruction of the cutinase family with fixed extant node locations. All 20 presented topologies failed rejection by the AU-test and are equally valid representations of the underlying sequence alignment. Extant tips of interest (*Thermobifida* cutinases, E5BBQ3, D4Q9N1, E9LVH9 and metagenomic assembled cutinases A0A2H5ZR95, G9B757 (LCC)) are labeled). Degradation of amorphous PET film by. (**B**) 20 extant and (**C**) 48 ancestral cutinases. The bulk soluble products of PET hydrolysis (TPA, MHET, BHET) are measured by absorbance at 260 nm after 16 hours incubation with the enzyme at 60 °C. Data are represented as the mean ± SEM (n = 3). (**D**) Phylogenetic tree 55, (**E**) 35 and (**F**) 10, with ancestors 35_442, 55_547 and 10_543 highlighted. Each ancestor belongs to equivalent nodes from independent phylogenetic topologies, and are the most recent common ancestor of LCC and TfCut2, extant cutinases with known PETase activity.

144 We selected 48 ancestral nodes from 20 different trees with homology to the most recent
145 common ancestor of LCC and *Tf*Cut2 for experimental characterization and comparison to
146 extant cutinases. Specifically, these nodes were chosen from the recent ancestors of the LCC
147 and *Tf*Cut2 lineages (or the most recent common ancestor of both), with at least a single
148 sequence sampled from each of the 20 distinct phylogenetic trees. Each ancestral sequence
149 was selected as the *maximum a posteriori* (MAP) sequence that maximizes the posterior
150 probability over the full-length of the reconstructed protein. The variants were expressed,
151 purified and tested for PETase activity. The soluble expression level of each variant was
152 measured using the Bradford assay (**Supplementary Figure 1**). PETase activity against
153 amorphous PET film was measured by UV absorbance at 260 nm to detect the soluble
154 products of PET hydrolysis after the removal of undigested film, including terephthalic acid
155 (TPA), mono(2-hydroxyethyl) terephthalate (MHET), and bis(2-hydroxyethyl) terephthalate
156 (BHET) (**Supplementary Figure 2**). Among the extant cutinases, the highest PETase
157 activities were observed for LCC (A_{260} nm = 0.34 ± 0.03), BhrPETase from bacterium HR29
158 (A_{260} nm = 0.49 ± 0.01), and a previously engineered variant of LCC with the mutations
159 F243I/D238C/S283C/Y127G (LCC ICCG)[6] (A_{260} nm = 0.54 ± 0.07), with other cutinases
160 showing lower activity (**Figure 1B**). Of the 48 ancestral variants, we observed PETase activity
161 for a number of ancestral cutinases from a diverse range of trees (**Figure 1C**). Several variants
162 (1_533, 35_442, 55_547, 70_439, 70_440, and 85_456) exhibited similar activity to the most
163 active extant cutinases, LCC and BhrPETase. From this group, we selected ancestors from
164 tree 35, node 442 (35_442; A_{260} nm = 0.37 ± 0.06) and tree 55, node 547 (55_547; A_{260} nm =
165 0.59 ± 0.09), for further investigation. Notably, these two ancestors belonged to equivalent
166 positions from two independent phylogenetic trees (Figure **1D-F**), representing the most
167 recent common ancestor of LCC and TfCut2, and sharing 98.5% sequence identity to one
168 another.
169
170 Within the dataset of 48 ancestral sequences, 12 represent the same phylogenetic node (the
171 most recent common ancestor of LCC and *Tf*Cut2) over 12 different phylogenetic
172 backgrounds. Of these, 9 exhibited PETase activity while 3 were inactive on PET.
173 Interestingly, the PETase ancestor 55_547 and the inactive ancestor 10_543 both represent
174 equivalent positions (the most recent common ancestor of *Tf*Cut2 and LCC) in their respective
175 phylogenetic backgrounds and differ by only 9/261 positions, yet 55_547 has activity against
176 PET and 10_543 does not. The functional differences between these sequences arise solely
177 from the topology of the phylogenetic tree used to reconstruct them and drastically alters how
178 the evolution of PETase activity could be inferred. For example, in the case of the 55_547
179 phylogeny, PETase activity appears to be a promiscuous ancestral trait that existed prior to
180 the discovery of extant PETases (such as LCC and *Thermobifida* cutinases), whereas the

181 10_543 phylogeny supports the contradictory hypothesis that PETase activity emerged
182 independently in LCC-like and *Thermobifida* PETase lineages from an ancestor without
183 PETase activity. As both topologies failed rejection by the approximately unbiased (AU)[41] test
184 and are statistically indifferent at representing the observed alignment data, it is not possible
185 to reject one of these hypotheses purely from a phylogenetic perspective. We also observe
186 no correlation between the mean posterior probability of an ancestor and its activity
187 (**Supplementary Figure 5**). This observation is somewhat counterintuitive, as the mean
188 posterior probability of a sequence, which is the statistical confidence in the identity of a
189 reconstructed ancestor, is often used to discriminate between poorly reconstructed sequences
190 (and hence likely to be less fit) and those that are likely to be functional and fit[40]. Together,
191 these results highlight the importance of sampling diverse phylogenetic backgrounds during
192 ASR when accessing the functional sequence space of a protein family as minor phylogenetic
193 incongruencies can translate into significant functional differences in (equivalent)
194 reconstructed ancestral sequences.
195
196 **Structural characterization and analysis of ancestral cutinases.**
197
198 A comparative structural and sequence analysis of inactive and active ancestors suggests
199 that PET hydrolysis appears to be a trait that is evolutionarily accessible from within the
200 cutinase background. Unlike the *I. sakaiensis* PETase, which emerged through conformational
201 optimization of the first- and second-shells *via* obvious selection within the active site[42–44],
202 PETase activity in the TfCut2 and LCC PETase lineages appears to emerge through non-
203 specific and likely neutral mutations that are often distal to the active site (**Figure 2A-C**).
204 Indeed, analysis of ancestral cutinase sequences reveals virtually no differences in the PET
205 binding sites between PETase active and inactive variants (**Supplementary Figure 6**).
206 Furthermore, mutations associated with a gain-of-function vary between the different
207 phylogenetic trees used to reconstruct the ancestral sequences. For example, ancestors
208 55_547 and 35_442 are each separated by 9 unique mutations from their closest relatives
209 without PETase activity (ancestors 10_543 with A15S, A36V, T49S, T92S, N109D, R114S,
210 N145R, I180V, S226A and 75_539 with A36V, T49D, T92S, M105Q, R114S, S124N, R167T,
211 P199S, A226S, respectively). Of these loss of function mutations, 3 are shared between either
212 background, 5 are unique and one is a reversion (S226A for 55_547, A226S for 35_442).
213 Intuitively, a combination (with at least one) of these mutations are required to be fixed in
214 either respective cutinase background to impart PETase activity. Similarly, ancestor 10_543
215 is separated by 8 mutations from its closest relative with PETase activity (70_439 with E28Q,
216 S49D, S124N, R145N, V180I, P199S, S215T, A226S); of the 8 mutations associated with
217 gain-of-function in the background of 10_543, only 3 are specifically shared with gain-of-

218 function mutations in 55_547. Nearly all functionally consequential mutations across
219 backgrounds are distal to the active site and PET binding pocket. This suggests that (i) there
220 are numerous (and diverse) molecular mechanisms by which PETase activity can emerge
221 from an ancestral cutinase without PETase activity, (ii) these mechanisms are not obviously
222 associated with a restructuring of the enzyme active site and (iii) PETase activity is readily
223 evolutionarily accessible within the cutinase family, consistent with recent observations of
224 PETases that have emerged from cutinase backgrounds[11,12].
225

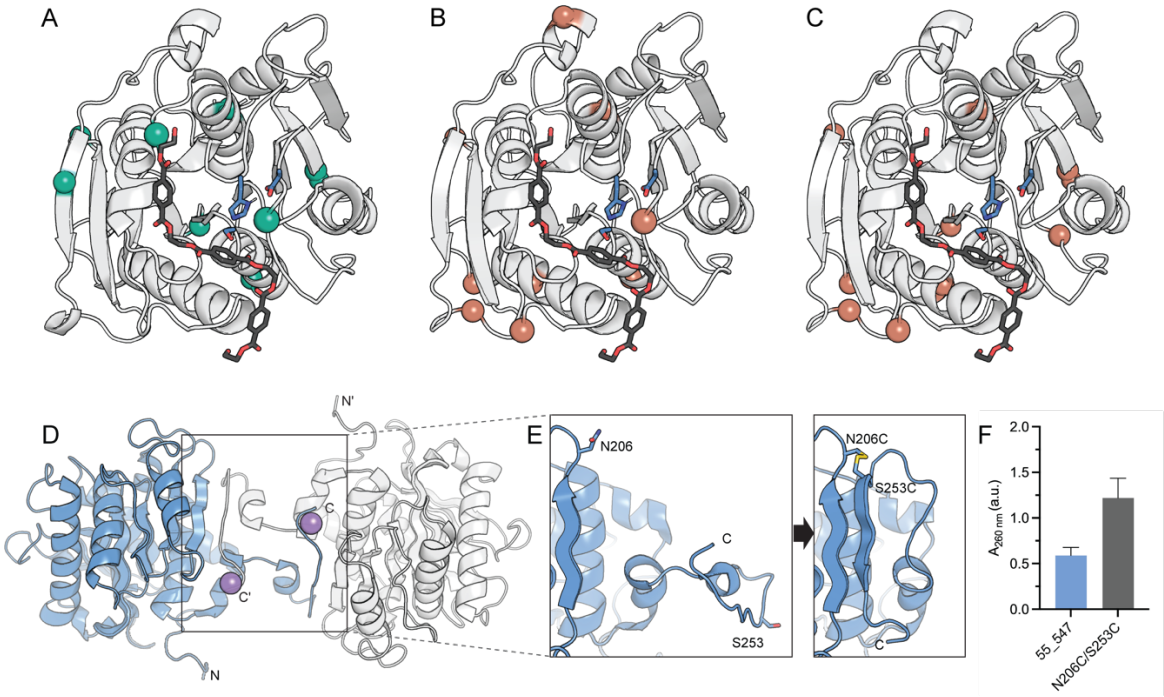

226

227 **Figure 2. Structural characterization of 55_547 and 35_442. A)** Positions of gain-of-function (GOF)
228 mutations in the inactive ancestor 10_543, and **B)** loss-of-function (LOF) mutations in the active
229 ancestors 55_547 and **C)** 35_442. GOF and LOF mutations are shown as teal and red spheres,
230 respectively. AlphaFold[45,46] was used to generate models of each ancestor. Most GOF/LOF mutations
231 are distal from the catalytic site residues (blue), and the putative PET binding site highlighted by the
232 docked 2HE-(MHET)3 ligand (black). Structural analysis of the active site residues H210, S132 and
233 D178 in ancestors 10_543, 55_547, and 35_442 shows uniform alignment, indicating that PETase
234 activity does not arise from modifications within the active sites (**SI. Figure 4**). **D)** Domain-swapped
235 homodimer observed in the crystal structure of ancestor 55_547 with two C-terminal strands swapped
236 (PDB 8ETX). The N- and C- termini of each subunit are indicated. The dimer is coordinated by sodium
237 ions (represented as purple spheres) in the crystal lattice. **E)** Positions on the flexible C-terminus of
238 ancestor 55_547 targeted for disulfide engineering, as shown in the crystal structure (left; PDB 8ETX),
239 resulting in the disulfide mutant N206C/S253C, as generated by AlphaFold[45,46] (right). The predicted
240 formation of an additional β-strand at the C-terminus, constrained by the disulfide bond, is shown. **F)**
241 PETase activity of ancestor 55_547 and the disulfide mutant N206C/S253C. The bulk soluble products
242 of PET hydrolysis (TPA, MHET, BHET) are measured by absorbance at 260 nm after 16 hours
243 incubation with the enzyme at 60 °C. Data are represented as the mean ± SEM (n = 3).
244

245 We next determined the crystal structures of two active ancestors, 35_442 (PDB 8ETY) and
246 55_547 (PDB 8ETX), and identified an additional pathway to optimizing PETase activity

247 beyond modification of the active site. Both ancestors crystallized in the C222 space group at
248 resolutions of 1.5 - 1.8 Å (**Supplementary Table 1**). Structural analysis revealed the formation
249 of domain-swapped dimers (**Figure 2D**). The observation of domain swapping, likely induced
250 by the high protein concentration in the crystallization conditions, suggests an intrinsic
251 flexibility of the C-terminus, a characteristic commonly observed in proteins previously
252 characterized to form domain-swapped dimers[47]. Given the flexible nature of the C-terminus,
253 it was hypothesized that introducing a disulfide bond to constrain this region into forming an
254 intramolecular β-sheet would enhance enzyme stability (**Figure 2E**). Furthermore, the chosen
255 site for the disulfide bond coincided with the predicted Ca^{2+}/Mg^{2+} binding site of the ancestors
256 based on homology to extant cutinases, a region previously targeted for disulfide bond
257 engineering in TfCut2 and LCC for improved thermostability and PETase activity[6,48,49]. We
258 introduced the disulfide mutation N206C/S253C to ancestor 55_547 and experimental
259 characterization of the resulting mutant demonstrated an approximately 2-fold improvement
260 in whole-cell activity ($A_{260\ nm}$ = 1.22 ± 0.22) (**Figure 2F**) and a 1.5-fold increase in soluble
261 expression levels compared to the 55_547 background determined by Bradford assay
262 (**Supplementary Figure 5**). In combination with our comparative analysis of the selected
263 inactive and active ancestors, the successful optimization of PETase activity via the
264 introduction of a disulfide bond distal to the active site illustrates that PETase activity within
265 the cutinase family can emerge and be enhanced through mechanisms that extend beyond
266 the structural reconfiguration of the active site. It is therefore likely that activity optimization is,
267 at least in part, being driven by thermodynamic and kinetic stabilization.
268
269

Alternate Reconstructions of Ancestral Cutinases 35_442 and 55_547.

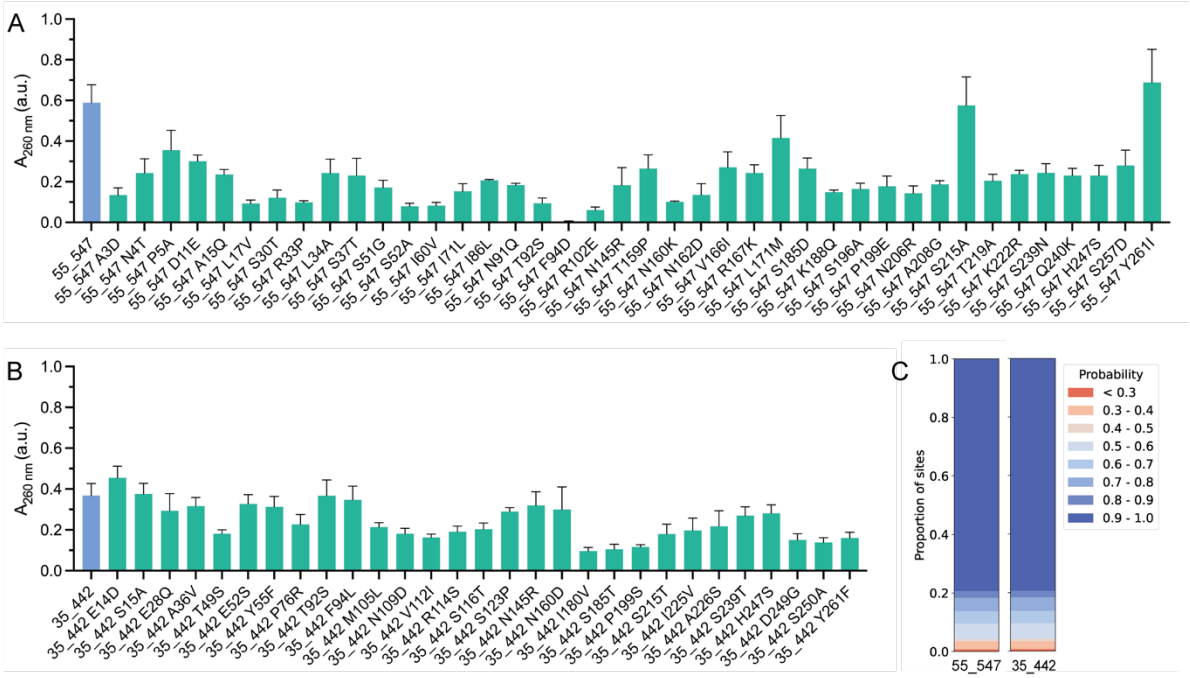

Figure 3. Alternate reconstructions and random recombinations of ancestral cutinases 35_442 and 55_547. Activity of alternate reconstructions of **A)** ancestor 55_547 and **B)** 35_442 against amorphous PET film. The bulk soluble products of PET hydrolysis (TPA, MHET, BHET) are measured by absorbance at 260 nm after 16 hours incubation with the enzyme at 60 °C. Data are represented as the mean ± SEM (n = 3). **C)** Posterior probability distributions for ancestors 55_547 and 35_442.

We next experimentally characterized all alternate sequences of ancestors 55_547 (40 mutants) and 35_442 (29 mutants) that individually sampled each mutation that had been ambiguously reconstructed. Here, we define ambiguity as any site where at least two amino acids are reconstructed with a posterior probability of >= 0.2. This provided a high resolution mutagenic map of the local sequence space around either of the ancestral PETase variants. Ambiguously reconstructed sites were spatially distributed over the protein and not localized to any specific functional area (**Supplementary Figure 7**). Having already established that the mean posterior probability of an ancestral sequence is a poor indicator of PETase activity (**Supplementary Figure 4B**) and that relatively minor changes in the cutinase sequence can drastically alter PETase activity, we hypothesized that the neighborhood of evolutionarily possible (albeit less probable) sequences may contain mutations that benefit PETase activity. This hypothesis was guided by recent ASR studies on the *I. sakaiensis* PETase branch of the cutinase phylogeny where PETase activity appeared to emerge transiently within ancestral lineages[50]. Experimental characterization revealed that all of the alternate reconstructions of ancestors 55_547 and 35_442 demonstrated PETase activity that was comparable (or reduced) to either respective ancestral background (**Figure 3A-B**).

295

296

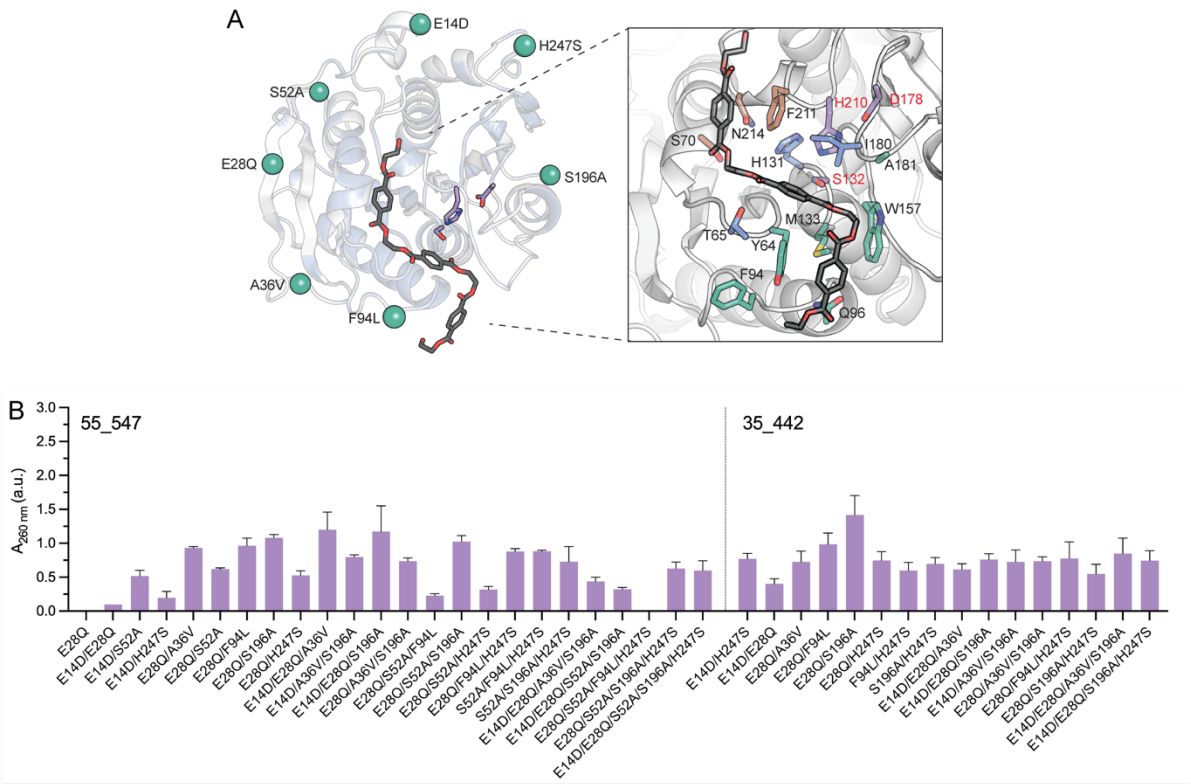

297

298 **Figure 4. PETase activities of recombined alternate reconstructions**. **A)** Structure of 35_442 and
299 55_547 aligned. Positions selected for recombination are highlighted as spheres. The docked pose of
300 2HE-$(MHET)_3$ is shown in a close-up of the binding and catalytic site, and residues that form the putative
301 PET binding site based on homology to LCC are shown. Residues comprising subsites -2 (green), -1
302 (blue) and +1 (brown) are highlighted. The catalytic residues Ser132-His210-Asp178 are also shown
303 (purple; red labels). **B)** Activity of recombined mutations from alternate reconstructions of 35_442 and
304 55_547 against amorphous PET film. The bulk soluble products of PET hydrolysis (TPA, MHET, BHET)
305 are measured by absorbance at 260 nm after 16 hours incubation with the enzyme at 60 °C. Data are
306 represented as the mean ± SEM (n = 3) and grouped based on mutations recombined in the background
307 of 55_547 (left) and 35_442 (middle).

308

309 A subset of randomly sampled combinations of single mutations from the alternate
310 reconstructions were selected to explore potential epistatic interactions and their impact on
311 PETase activity. The 7 selected mutations, E14D, E28Q, A36V, S52A (in 55_547), F94L,
312 S196A, and H247S, were recombined in various combinations from 2 to 5 point mutations in
313 the background of 35_442 and 55_547. E28Q, A36V, S52A, S196A, and H247S are surface
314 mutations, distal from the catalytic and putative PET binding site (**Figure 4A**). In contrast,
315 F94L is positioned within the PET binding site, as deduced from docking of 2HE-$(MHET)_3$ into
316 both 35_442 and 55_547 (**Figure 4A**), as well as structural homology to previously predicted
317 PET binding sites in LCC. As single mutations, E14D, E28Q, A36V, F94L and H247S were
318 considered neutral based on PETase activity relative to the 35_442 background, while S52A
319 and S196A exhibited decreased activity relative to 55_547. In our experimental

320 characterization, we identified 24 recombined variants with increased PETase activity relative
321 to their ancestral background (**Figure 4B**). Specifically, 10 recombined variants in the
322 background of 55_547 showed increased PETase activity, with the most active being
323 E14D/E28Q/A36V (A_{260} nm = 1.20 ± 0.26), E28Q/S196A (A_{260} nm = 1.08 ± 0.05), and
324 E28Q/S52A/S196A (A_{260} nm = 1.03 ± 0.09). Similarly, 14 recombinations in the background
325 of 35_442 demonstrated increased activity, with the most active being E28Q/S196A (A_{260} nm
326 = 1.42 ± 0.29), E28Q/F94L (A_{260} nm = 0.99 ± 0.17), and E14D/H247S (A_{260} nm = 0.77 ± 0.08).
327 Interestingly, we identified 17 recombined variants that exhibited improved PETase activity
328 relative to LCC ICCG, the most active extant variant in the study, with 35_442 E28Q/S196A,
329 displaying ~2.5-fold higher activity.
330
331 The mutational analysis of the recombined variants highlighted E28Q as a key mutation,
332 present in 14 of the 17 variants that demonstrated enhanced activity compared to the
333 engineered LCC ICCG variant. This suggests a positive effect of E28Q on PETase activity;
334 however, this was only observed in the presence of other mutations from the recombinations.
335 The context dependence of E28Q is especially significant when considering the double
336 mutation E28Q/S196A, which was among the most active in both ancestral backgrounds.
337 When assessed independently in the 55_547 background, the E28Q mutation adversely
338 affected activity (A_{260} nm = 0.00 ± 0.00), and the S196A mutation similarly led to a reduction
339 in activity relative to the ancestor (A_{260} nm = 0.16 ± 0.02). However, the combination of these
340 mutations resulted in a significant increase in activity beyond the additive effects of the single
341 mutations (A_{260} nm = 1.08 ± 0.05), indicative of positive epistatic interactions.
342
343 **Ruggedness analysis reveals epistasis in recombined mutations.**
344
345 We next analyzed the topology of the PETase fitness landscape over the 196 cutinase
346 sequences characterized in this study. This was done both to build a holistic overview of
347 PETase evolution and function in the cutinase family and to assess the effectiveness of this
348 approach in exploring new-to-nature fitness peaks across functional sequence space. To
349 achieve this, we embedded cutinase sequences as nodes in a network graph where edges
350 connect each node to its *k* nearest (Euclidean) neighbors. The scheme used to embed
351 sequences therefore dictates the topology of the network graph. When this is the one-hot
352 encoding (OHE), the Euclidean distance between nodes in the network graph is proportional
353 to the number of mutations between the sequences they represent. The OHE graph network
354 therefore captures PETase activity as a function of the mutations between sequences when
355 the signal over the graph is the measured PETase activity (**Figure 5A**).
356

357 Encoding protein sequences as the hidden states of a PLM can capture comparatively richer
358 features than the OHE[29,30], albeit at the cost of interpretability over the network graph[36].
359 Euclidean distances in the latent space of a representation model may share no interpretable
360 relationship with equivalent Euclidean distances in the OHE space, therefore confounding the
361 interpretation of PETase activity over the network graph to non-linear distances instead of
362 simple mutational distances.
363
364 We embedded all characterized cutinases in a OHE basis and visualized the resulting
365 landscape in 2 dimensions with t-distributed stochastic neighbor embedding (tSNE)
366 dimensionality reduction. In this space, ancestral and extant cutinases form homogenous,
367 random clusters (**Figure 5A**). The alternate reconstructions of ancestors 55_547 and 35_442
368 and their recombinations are grouped as closely connected clusters around their respective
369 ancestral backgrounds. Despite their comparable PETase activity, sequences in both
370 backgrounds are resolved as independent components that share few direct edge
371 connections, suggesting that the PETase fitness landscape is multi-modal (i.e. there are
372 multiple solution spaces to competent PETase activity) when considering only naive, residue-
373 wise OHE sequence embeddings.
374
375 We then reconstructed the PETase fitness landscape in a learned representation space. To
376 ensure that local features of the cutinase sequence space were captured by a PLM, we used
377 a recently described method of local ancestral sequence embedding (LASE)[36]. In brief, LASE
378 trains a small and family-specific deep learning model on ancestrally reconstructed sequence
379 datasets. The features learned by LASE capture the functional properties of proteins, such as
380 catalytic efficiency, in a non-linear space that is not interpretable with simple mutational
381 distances. Embedding in LASE can therefore reveal topological features of the fitness map
382 that are obfuscated in an OHE embedding.
383
384 Sequences in the LASE embedding space cluster according to their relative fitness and how
385 they were sampled (e.g. extant, ancestral, alternate or recombined; **Figure 5B**). For example,
386 all point mutations from alternate reconstructions and recombinations group together in a
387 single connected component in the LASE space, irrespective of the genetic background
388 (ancestors 55_547 or 35_442) they were introduced into. Moreso, ancestral and extant
389 sequences cluster into disconnected components, despite their often high degree of site-wise
390 sequence similarity. Indeed, the LASE representation space is highly structured relative to the
391 OHE space, where ancestral and extant sequences co-occur across distinct identity groups in
392 the network graph. This indicates that our sequence sampling strategy is highly structured and

systematic over an evolutionarily informative representation space, while appearing somewhat random in the OHE space.

Finally, we used a graph signal processing approach to quantify ruggedness in the cutinase PET fitness landscape. We define ruggedness as the non-linearity between the fitness of a sequence and its neighbors in the network graph. We use the Dirichlet energy of the graph, which describes the non-linearity of a signal over a graph, to measure this[36,51,52]. In order to make the Dirichlet energy interpretable as a node-wise local quantity, we calculate it over each subgraph in the network defined by an edge-length of exactly 1, thus reducing its interpretation to the deviation from linearity a node demonstrates relative only to its immediate neighbors; the fitness signal over the network graph changes as a linear function (i.e. is smooth) over nodes of the graph that are characterized by low local DEs. The local Dirichlet energy is therefore a descriptor of how confounded by epistasis a sequence is. This analysis revealed that the fitness landscape is most rugged over the cutinase variants with the greatest PETase activity. Indeed, the node with the single highest local Dirichlet energy is also the fitness peak (ancestor 55_547_E28Q/S196A). Importantly, this was true for both OHE and LASE network graphs (**Figure 5C**; **Supplementary Figure 9**), indicating that the combinatorial mutations E28Q/S196A in the 55_547 background would be unlikely to be introduced through a stepwise mutagenesis approach due to the relatively low activity of each single mutation in isolation. Together, these analyses demonstrate that mASR can effectively guide protein engineering by discovering evolutionary features that are not immediately apparent, and can help navigate rugged regions of sequence space to find fit enzyme variants that are not rationally obvious.

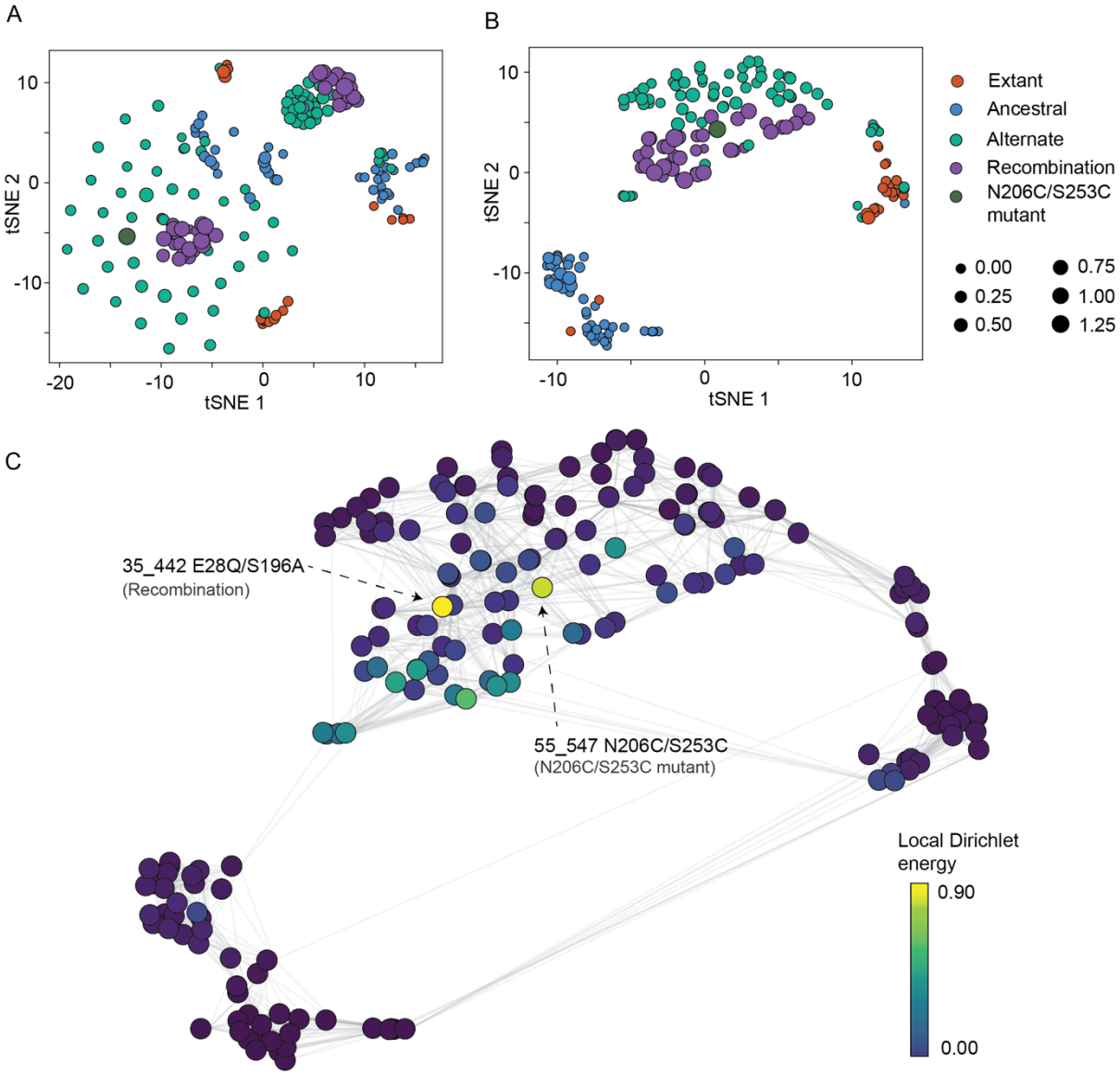

Figure 5. Analysis and regression on PETase sequence space. PETase sequences were represented in **A)** OHE- and **B)** LASE-forms and projected into a 2-dimensional space with tSNE. Colour represents design stage and size represents activity ($A_{260\ nm}$ (a.u.)). The OHE and LASE sequence data was then used to train regression models. **C)** The local Dirichlet energy for each variant was determined over subgraphs that include the variant's immediate neighbors as determined by kNN. Edges connect variants that were found to be neighbors and color represents the local Dirichlet energy calculated.

Discussion

In our investigation into the evolutionary sequence space of bacterial cutinases with PETase activity, we employed multiplexed ASR[36] to enhance our exploration. This method allowed us to reconstruct and analyze ancestral cutinases across 20 diverse phylogenetic topologies, moving beyond the constraints of a single-tree perspective. Our experimental characterizations of 20 extant and 48 ancestral cutinases unveiled a wide spectrum of activities against amorphous PET film (A_{260} nm = 0.00 - 0.59). Of particular interest were two ancestors, 35_442 (A_{260} nm = 0.37 ± 0.06) and 55_547 (A_{260} nm = 0.59 ± 0.09), each representing the most recent common ancestor of LCC[13] and TfCut2[5] on independent trees and exhibiting similar activity to the most active extant cutinases, LCC (A_{260} nm = A_{260} nm = 0.34 ± 0.03) and BhrPETase (A_{260} nm = 0.49 ± 0.01). Notably, the use of mASR was crucial in uncovering the variability of ancestrally reconstructed sequences, as it revealed that equivalent nodes from independent phylogenetic topologies exhibited highly varied activity despite all topologies being equally valid representations of the underlying sequence alignment based on the AU-test. While some ancestors were inactive, others showed significant PETase activity comparable to characterized extant PETases. These observations highlight the utility of the mASR method in improving both the success and robustness of ASR applications in protein engineering. By embracing a wider array of evolutionary scenarios, mASR allowed for a more comprehensive and reliable identification of functional sequences relative to a single-tree approach. Multiplexed ASR may therefore become an important component of ASR- and evolutionary-guided enzyme design strategies in the future.

Our sequence and structural analysis of active and inactive ancestral cutinases provided insights on the evolutionary emergence of PETase activity in the cutinase family. In particular, our findings suggest that PETase activity in the TfCut2 and LCC PETase lineages has emerged through neutral mutations that are distal to the active site, rather than specific changes localized to the active site itself, as observed in the evolution of *I. sakaiensis* PETase[37]. Our detailed examination of ancestors 35_442 and 55_547, along with their closest inactive counterparts, highlighted unique gain-of-function mutations leading to PETase activity from these distinct phylogenetic backgrounds. These findings imply the existence of multiple, distinct evolutionary pathways for acquiring PETase functionality and indicate that PETase activity is readily accessible within the cutinase family.

Our structural analysis also revealed the formation of domain-swapped dimers between adjacent symmetry mates in the crystal structures of the ancestral variants 35_442 and

460 55_547. While possibly an artifact of the crystallization conditions, this observation suggests
461 a certain degree of structural flexibility in the C-terminus of these ancestors even in solution.
462 Based on this observation, we introduced a disulfide bond in the C-terminus of ancestor
463 55_547 that coincided with the predicted Ca^{2+}/Mg^{2+} binding site, a strategy homologous to
464 similar successful modifications in TfCut2 and LCC that were observed to improve stability
465 and activity[6,48,49]. Indeed, the introduction of the disulfide N206C/S253C resulted in a variant
466 of 55_547 with an approximately 2-fold improvement in whole-cell activity and 1.5-fold
467 improvement in soluble expression relative to the background ancestor.
468
469 We deepened our exploration of the evolutionary sequence space of the cutinase family by
470 addressing ambiguously reconstructed positions in the initial mASR. Ambiguous positions
471 were identified based on a posterior probability threshold of ≥ 0.2 for the second most probable
472 residue. Introducing these 69 alternate reconstructions as single mutations into 35_442 and
473 55_547, we observed that most mutations were either neutral or decreased PETase activity
474 relative to the ancestral background. However, when we recombined a random subset of the
475 alternate reconstructions, we observed several recombinations in the background of both
476 35_442 (E28Q/S196A) and 55_547 (E14D/E28Q/A36V) that displayed increased PETase
477 activity, not only relative to the initial ancestors, but also to an engineered variant of LCC with
478 enhanced activity, $LCC^{ICCG\ 6}$. Notably, the most active recombinations exhibited activity
479 improvements that exceeded the additive effects predicted from their individual mutations,
480 highlighting positive epistatic interactions that contribute to their PETase activity.
481
482 To complement our experimental investigations, we modeled the sequence-fitness landscape
483 of all 196 cutinase sequences characterized in our study, employing a graph signal processing
484 approach that elucidates the complex topology of the PETase fitness landscape. This
485 methodology involved embedding cutinase sequences as nodes in a network graph, where
486 each node was connected to its *k* nearest (Euclidean) neighbors, thereby enabling a direct
487 comparison between two embedding schemes, OHE and LASE. While OHE provides a
488 straightforward mutational distance metric between sequences, it often oversimplifies the
489 nuanced relationship between sequence variation and function. In contrast, LASE, by training
490 a family-specific deep learning model on our dataset of ancestrally reconstructed sequences,
491 captures the functional properties of proteins in an abstract manner, revealing non-linear
492 sequence-activity relationships that are obscured in OHE representations.
493
494 Using LASE to map the sequence-fitness landscape, we highlighted iterative improvements
495 in PETase activity throughout the different phases of our sequence exploration of the cutinase
496 family. This embedding not only facilitated a deeper understanding of the functional

implications of sequence variation but also allowed us to identify clusters of sequences with similar functional profiles, regardless of their evolutionary background. Moreover, our analysis of the fitness landscape's ruggedness via LASE provided new insights into the role of epistasis in PETase activity. The local Dirichlet energy calculations revealed that sequences with the highest PETase activity were associated with the greatest ruggedness, suggesting that the most functionally optimized variants emerge from complex interplays of multiple mutations rather than from linear accumulations of beneficial single mutations. This observation highlights the significance of epistatic interactions in driving the evolutionary innovation of PETase activity, illustrating that successful enzyme variants often lie in regions of the fitness landscape that are not readily accessed through single mutational steps, but can be accessed using evolutionarily-guided approaches, such as mASR.

510 **Materials and Methods**

511

512 **Ancestral sequence reconstruction**. 1000 sequences were collected from the NCBI non-
513 redundant (nr) database with blast using LCC (UniProt: G9BY57) as seed and an e-value
514 cutoff of 1e-5. Sequence redundancy was removed to 90% ID in CD-HIT[53]. Signal peptides
515 were deleted using SignalP4.0[54]. Alignment was performed using the GINSI protocol of
516 MAFFT[55]. 100 replicates of independent model parameterization and tree search (default
517 parameters) were performed using IQTREE2[56] on the NCI GADI supercomputer. The
518 sequence evolution model was parameterized using ModelFinder[57], as implemented in
519 IQTREE2. Branch supports were determined as the ultrafast bootstrap approximation[38]
520 calculated to 1000 replicates, as implemented in IQTREE2. The Approximately unbiased test[41]
521 was conducted to 10000 replicates for all ML topologies. Empirical Bayesian ASR was
522 performed on 20 of the 100 trees that failed rejection by the AU test in CodeML[39] using the
523 ML replacement matrix (LG)[58] with rates modeled as a discrete gamma parameterized with 4
524 rate categories.

525

526 **Small-scale protein expression and purification**. Plasmids were transformed by heat shock
527 into chemically competent BL21(DE3) *E. coli* cells and plated onto Lysogeny broth (LB) agar
528 supplemented with 100 µg/mL kanamycin and incubated at 37 °C overnight. A single colony
529 was used to inoculate 1.5 mL autoinduction media supplemented with 100 µg/mL kanamycin
530 in a 2.2 mL 96-well deep well block and grown at 1050 rpm at 37 °C for 5 hours, followed by
531 room temperature (RT; 25 °C) for 16 hours.

532

533 Cells were harvested by centrifugation at 2000 x *g* for 15 minutes at RT and resuspended in
534 Lysis Buffer (1X BugBuster® Protein Extraction Reagent (Merck-Millipore), 20 mM Tris, 300
535 mM NaCl, 1 U/ml Turbonuclease (Sigma) pH 8). The cell suspension was left to incubate at
536 RT for 20 minutes with gentle shaking. The lysate was separated from the insoluble cell debris
537 by centrifugation at 2250 x g for 1 hour at RT.

538

539 The clarified lysate was then diluted with 100 µl of Equilibration Buffer (20 mM Tris, 300 mM
540 NaCl pH 8) and purified by nickel-charged IMAC using a 96-well HisPurTM Ni-NTA Spin Plate
541 (ThermoFisher Scientific) equilibrated in Equilibration Buffer, washing the sample three times
542 with 250 µl of Wash Buffer (20 mM Tris, 300 mM NaCl, 10 mM imidazole pH 8) and eluting
543 with 250 µl of Elution Buffer (20 mM Tris, 300 mM NaCl, 150 mM imidazole pH 8). All
544 centrifugation steps following addition of Wash or Elution Buffer were at 1000 x *g* for 1 minute
545 at RT. The eluate was stored at 4 °C. Bradford assay was used to quantify the soluble
546 expression levels post-purification (**Supplementary Figure 1**).

547
548 **UV absorbance assay for PET-degrading activity**. For purified protein from 96-well
549 expression and purification, 15 µl of the eluate from the 96-well Ni-NTA purification and 285
550 µl of Reaction Buffer (50 mM Bicine pH 9) was added to a clear 96-well plate. For purified
551 protein from large-scale expression and purification, 300 µl of 100 nM enzyme in Reaction
552 Buffer was added to a clear 96-well plate. A single disk of amorphous PET (Goodfellow
553 ES301445) with 4 mm diameter and 0.25 mm thickness was added to each well. The plate
554 was incubated at 60 °C for 16 hours. Following incubation, 100 µl of the reaction solution was
555 transferred to a clear UV-transparent 96-well plate and the absorbance was measured
556 between 240 to 300 nm in 10 nm steps using the Epoch Microplate Spectrophotometer
557 (BioTek) (**Supplementary Figure 2**). For comparison of activity of all variants, the absorbance
558 at 260 nm was used. Assays were repeated in triplicate for each variant.
559
560 **Assay data processing.** To correct for possible systematic error between replicate data
561 points, the mean absorbance at 260 nm for each replicate was determined. Using the mean
562 absorbance, a scaling coefficient was assigned to the replicates with the lowest and highest
563 mean values such that the mean of the scaled absorbance values equaled the mean of the
564 replicate with the mid-range mean value. To ensure scaling improved consistency between
565 replicates, correlograms of the data before (**Supplementary Figure 3**) and after
566 (**Supplementary Figure 4**) scaling were produced to confirm the monotonic (rank) correlation
567 between replicates was preserved.
568
569 **Cloning of TEV-PETase variants for crystallography studies.** Primer pairs containing the
570 DNA sequence for the TEV cleavage site (5'-GAAAACCTGTATTTTCAAAGC-3') were
571 constructed, specific to each PETase variant. PCR was performed using these primers and
572 PETase variant genes to create mutant fragments. These fragments were reassembled using
573 Gibson Assembly[59] and checked through Sanger sequencing to ensure the TEV cleavage site
574 was correctly introduced.
575
576 **Large scale protein expression and purification.** The TEV-PETase ancestral variants
577 plasmids were transformed using electroporation into electrocompetent E. cloni® cells
578 (Lucigen) and plated onto LB agar supplemented with 100 µg/mL kanamycin. The plates were
579 incubated overnight at 37 °C. A single colony was inoculated into a 10 mL solution of LB media
580 with 100 µg/mL kanamycin and incubated overnight at 37 °C and 180 rotations per minute
581 (rpm). This liquid starter culture was then added to 1 L of autoinduction media[60] (6 g Na_2HPO_4,
582 3 g KH_2PO_4, 20 g tryptone, 5 g yeast extract, 5 g NaCl, 10 mL of 60% (v/v) glycerol, 5 mL of
583 10% (w/v) glucose, and 25 mL of 8% (w/v) lactose) with 100 µg/mL kanamycin and incubated

584 for 24 hours at room temperature and 180 rpm. The cells were separated from the media by
585 centrifugation at 5000 × g for 15 minutes at 4 °C and resuspended in lysis buffer (400 mM
586 NaCl, 25 mM imidazole, 1 U/mL Turbonuclease (Sigma), and 50 mM Tris-HCl pH 8.0). The
587 resuspended cell solution was lysed using two rounds of sonication at 50% power and pulse
588 time for 5 minutes, with 5 minutes on ice between sonication steps. Next, the sample was
589 centrifuged at 32000 × g for 60 minutes at 4 °C, and the soluble cell solution was separated
590 from the insoluble cell material and filtered through a 0.45 µm pore size filter. The filtered
591 soluble cell solution was passed through an equilibrated Nickel-charged IMAC using a 5 mL
592 HisTrap HP (GE Healthcare Life Sciences) in Lysis Buffer. The protein bound to the column
593 was eluted using elution buffer (400 mM NaCl, 500 mM imidazole, and 50 mM Tris-HCl pH
594 8.0). The protein sample was buffer exchanged to TEV reaction buffer (100 mM NaCl, 0.5 mM
595 EDTA, 1 mM DTT, 1% (v/v) glycerol, and 50 mM Tris-HCl pH 8.0) using a PD-10 desalting
596 column and diluted to 50 mL in this buffer. A 1 mL solution containing 1 mg/ml of purified TEV
597 protease was added and incubated at room temperature overnight. The cleaved sample was
598 passed through an equilibrated Nickel-charged IMAC using a 5 mL HisTrap HP (GE
599 Healthcare Life Sciences), and the flowthrough was collected. This flowthrough was
600 concentrated using the 3 kDa Amicon® ultra 15 mL centrifugal filters and filtered through a
601 0.22 µm filter. Finally, the cleaved protein was purified to homogeneity using size-exclusion
602 chromatography, and the HiLoad 26/600 Superdex 200 column (GE Healthcare Life Sciences)
603 was equilibrated in size-exclusion buffer (150 mM NaCl, 25 mM HEPES pH 7.5).
604
605 **Protein crystallisation and structure determination.** Proteins were concentrated using the
606 3 kDa Amicon® ultra 15 mL centrifugal filters to 15-36 mg/ml and crystallized in 20% (w/v)
607 PEG 3350 alongside 0.2 M salt and BisTris buffer solution. Specifically, ancestor 55_547 in
608 0.2 M sodium/potassium tartrate, 0.1 M BisTris propane pH 7.5 and 20% (w/v) PEG 3350; and
609 ancestor 35_442 in 0.2 M sodium malonate, 0.1 M BisTris propane pH 6.5 and 20% (w/v) PEG
610 3350. The X-ray diffraction data were collected on the MX2 beamline at the Australian
611 Synchrotron[61]. The data was processed using XDS[62], and the phase problem was resolved
612 with molecular replacement using the PETase WT structure (PDB: 6EQE) as the search
613 model. The ligands and solvent molecules were removed and then used as the search model
614 part of Phaser (CCP4)[63]. The structure was refined using phenix.refine[64] through multiple
615 iterative steps, and rebuilt each time with Coot[65]. The structures of ancestors 55_547 and
616 35_442 were deposited in the protein data bank under the PDB ID of 8ETX and 8ETY,
617 respectively.
618
619 **Protein sequence representations.** To analyze PETase sequence space One-hot
620 embeddings (OHE) and Learned Ancestral Sequence Embeddings (LASE) were made. To

621 produce OHE, aligned PETase sequences were converted into a (20×267) vectors where
622 gaps were represented as a zero vector of length 20. The LASE embedding model was
623 implemented as a Transformer in PyTorch 2.0.1 as previously described[36], with three encoder
624 blocks with 2-headed multihead attention (64 dimensions) and a feed-forward fully-connected
625 layer (128 dimensions). The LASE embedding model was trained with a masking percent of
626 15%, over 100 epochs with a batch size of 32 using the Adam optimizer. Loss was determined
627 as the categorical cross entropy loss. Performance over training was assessed with perplexity
628 and categorical accuracy (**Supplementary Figure 8**).
629
630 **Local Dirichlet energy calculations.**
631 To estimate the local ruggedness of each PETase variant, the k-nearest neighbors of each
632 node were used to produce a KNN sub-graph for each variant with scikit-learn 1.2.1. The kNN
633 sub-graphs were made symmetric by defining an edge in either direction to be a single edge.
634 The dirichlet energy was calculated as previously described[52,66]:
635
636 $$\lambda_m = 1/N\ y^T L y$$
637
638 Where, λ_m is normalized dirichlet energy, N, the number of variants in the sub-graph, y, the
639 activity (absorbance) of each variant and L the graph Laplacian operator of the adjacency
640 matrix of each kNN sub-graph.
641
642 **Acknowledgements**

643 This research was undertaken in part using the MX2 beamline at the Australian Synchrotron,
644 part of ANSTO, and made use of the Australian Cancer Research Foundation (ACRF)
645 detector.

646
647 **Availability**
648 The code for model training and analysis is available on GitHub:
649 https://github.com/RSCJacksonLab/cutinase_lase
650 Deposited crystal structures are available on the Protein Data Bank under accession IDs
651 8ETY and 8ETX.
652
653 **Note**
654
655 The authors declare the following competing financial interest(s): C.J.J., V.V., M.A.S., R.G.,
656 D.M., J.S., A.M.D., and J.T. hold equity in the plastic recycling company, Samsara Eco.

References

(1) *Plastic pollution is growing relentlessly as waste management and recycling fall short, says OECD*. https://www.oecd.org/environment/plastic-pollution-is-growing-relentlessly-as-waste-management-and-recycling-fall-short.htm (accessed 2023-12-16).

(2) OECD. Global Plastics Outlook, 2022. https://www.oecd-ilibrary.org/content/publication/de747aef-en.

(3) Zhu, B.; Wang, D.; Wei, N. Enzyme Discovery and Engineering for Sustainable Plastic Recycling. *Trends Biotechnol.* **2022**, *40* (1), 22–37. https://doi.org/10.1016/j.tibtech.2021.02.008.

(4) Egmond, M. R.; de Vlieg, J. Fusarium Solani Pisi Cutinase. *Biochimie* **2000**, *82* (11), 1015–1021. https://doi.org/10.1016/s0300-9084(00)01183-4.

(5) Herrero Acero, E.; Ribitsch, D.; Steinkellner, G.; Gruber, K.; Greimel, K.; Eiteljoerg, I.; Trotscha, E.; Wei, R.; Zimmermann, W.; Zinn, M.; Cavaco-Paulo, A.; Freddi, G.; Schwab, H.; Guebitz, G. Enzymatic Surface Hydrolysis of PET: Effect of Structural Diversity on Kinetic Properties of Cutinases from Thermobifida. *Macromolecules* **2011**, *44* (12), 4632–4640. https://doi.org/10.1021/ma200949p.

(6) Tournier, V.; Topham, C. M.; Gilles, A.; David, B.; Folgoas, C.; Moya-Leclair, E.; Kamionka, E.; Desrousseaux, M.-L.; Texier, H.; Gavalda, S.; Cot, M.; Guémard, E.; Dalibey, M.; Nomme, J.; Cioci, G.; Barbe, S.; Chateau, M.; André, I.; Duquesne, S.; Marty, A. An Engineered PET Depolymerase to Break down and Recycle Plastic Bottles. *Nature* **2020**, *580* (7802), 216–219. https://doi.org/10.1038/s41586-020-2149-4.

(7) Carniel, A.; Valoni, É.; Nicomedes, J.; Gomes, A. da C.; Castro, A. M. de. Lipase from *Candida Antarctica* (CALB) and Cutinase from *Humicola Insolens* Act Synergistically for PET Hydrolysis to Terephthalic Acid. *Process Biochem.* **2017**, *59*, 84–90. https://doi.org/10.1016/j.procbio.2016.07.023.

(8) von Haugwitz, G.; Han, X.; Pfaff, L.; Li, Q.; Wei, H.; Gao, J.; Methling, K.; Ao, Y.; Brack, Y.; Mican, J.; Feiler, C. G.; Weiss, M. S.; Bednar, D.; Palm, G. J.; Lalk, M.; Lammers, M.; Damborsky, J.; Weber, G.; Liu, W.; Bornscheuer, U. T.; Wei, R. Structural Insights into (Tere)Phthalate-Ester Hydrolysis by a Carboxylesterase and Its Role in Promoting PET Depolymerization. *ACS Catal.* **2022**, *12* (24), 15259–15270. https://doi.org/10.1021/acscatal.2c03772.

(9) Gamerith, C.; Vastano, M.; Ghorbanpour, S. M.; Zitzenbacher, S.; Ribitsch, D.; Zumstein, M. T.; Sander, M.; Herrero Acero, E.; Pellis, A.; Guebitz, G. M. Enzymatic Degradation of Aromatic and Aliphatic Polyesters by P. Pastoris Expressed Cutinase 1 from

692 Thermobifida Cellulosilytica. *Front. Microbiol.* **2017**, *8*, 938.
693 https://doi.org/10.3389/fmicb.2017.00938.
694 (10) Silva, C.; Da, S.; Silva, N.; Matamá, T.; Araújo, R.; Martins, M.; Chen, S.; Chen, J.; Wu,
695 J.; Casal, M.; Cavaco-Paulo, A. Engineered Thermobifida Fusca Cutinase with Increased
696 Activity on Polyester Substrates. *Biotechnol. J.* **2011**, *6* (10), 1230–1239.
697 https://doi.org/10.1002/biot.201000391.
698 (11) Amaral-Zettler, L. A.; Zettler, E. R.; Mincer, T. J. Ecology of the Plastisphere. *Nat. Rev.*
699 *Microbiol.* **2020**, *18* (3), 139–151. https://doi.org/10.1038/s41579-019-0308-0.
700 (12) Qi, X.; Ji, M.; Yin, C.-F.; Zhou, N.-Y.; Liu, Y. Glacier as a Source of Novel Polyethylene
701 Terephthalate Hydrolases. *Environ. Microbiol.* **2023**, *25* (12), 2822–2833.
702 https://doi.org/10.1111/1462-2920.16516.
703 (13) Sulaiman, S.; Yamato, S.; Kanaya, E.; Kim, J.-J.; Koga, Y.; Takano, K.; Kanaya, S.
704 Isolation of a Novel Cutinase Homolog with Polyethylene Terephthalate-Degrading
705 Activity from Leaf-Branch Compost by Using a Metagenomic Approach. *Appl. Environ.*
706 *Microbiol.* **2012**, *78* (5), 1556–1562. https://doi.org/10.1128/AEM.06725-11.
707 (14) Ronkvist, Å. M.; Xie, W.; Lu, W.; Gross, R. A. Cutinase-Catalyzed Hydrolysis of
708 Poly(Ethylene Terephthalate). *Macromolecules* **2009**, *42* (14), 5128–5138.
709 https://doi.org/10.1021/ma9005318.
710 (15) Vertommen, M. A. M. E.; Nierstrasz, V. A.; Veer, M. van der; Warmoeskerken, M. M. C.
711 G. Enzymatic Surface Modification of Poly(Ethylene Terephthalate). *J. Biotechnol.* **2005**,
712 *120* (4), 376–386. https://doi.org/10.1016/j.jbiotec.2005.06.015.
713 (16) Akutsu-Shigeno, Y.; Adachi, Y.; Yamada, C.; Toyoshima, K.; Nomura, N.; Uchiyama, H.;
714 Nakajima-Kambe, T. Isolation of a Bacterium That Degrades Urethane Compounds and
715 Characterization of Its Urethane Hydrolase. *Appl. Microbiol. Biotechnol.* **2006**, *70* (4),
716 422–429. https://doi.org/10.1007/s00253-005-0071-1.
717 (17) Ma, Y.; Yao, M.; Li, B.; Ding, M.; He, B.; Chen, S.; Zhou, X.; Yuan, Y. Enhanced
718 Poly(Ethylene Terephthalate) Hydrolase Activity by Protein Engineering. *Engineering*
719 **2018**, *4* (6), 888–893. https://doi.org/10.1016/j.eng.2018.09.007.
720 (18) Cui, Y.; Chen, Y.; Liu, X.; Dong, S.; Tian, Y.; Qiao, Y.; Mitra, R.; Han, J.; Li, C.; Han, X.;
721 Liu, W.; Chen, Q.; Wei, W.; Wang, X.; Du, W.; Tang, S.; Xiang, H.; Liu, H.; Liang, Y.;
722 Houk, K. N.; Wu, B. Computational Redesign of a PETase for Plastic Biodegradation
723 under Ambient Condition by the GRAPE Strategy. *ACS Catal.* **2021**, *11* (3), 1340–1350.
724 https://doi.org/10.1021/acscatal.0c05126.
725 (19) Son, H. F.; Cho, I. J.; Joo, S.; Seo, H.; Sagong, H.-Y.; Choi, S. Y.; Lee, S. Y.; Kim, K.-J.
726 Rational Protein Engineering of Thermo-Stable PETase from Ideonella Sakaiensis for
727 Highly Efficient PET Degradation. *ACS Catal.* **2019**, *9* (4), 3519–3526.
728 https://doi.org/10.1021/acscatal.9b00568.

(20) Wei, R.; Oeser, T.; Schmidt, J.; Meier, R.; Barth, M.; Then, J.; Zimmermann, W. Engineered Bacterial Polyester Hydrolases Efficiently Degrade Polyethylene Terephthalate Due to Relieved Product Inhibition. *Biotechnol. Bioeng.* **2016**, *113* (8), 1658–1665. https://doi.org/10.1002/bit.25941.

(21) Hellesnes, K. N.; Vijayaraj, S.; Fojan, P.; Petersen, E.; Courtade, G. Biochemical Characterization and NMR Study of a PET-Hydrolyzing Cutinase from Fusarium Solani Pisi. *Biochemistry* **2023**, *62* (8), 1369–1375. https://doi.org/10.1021/acs.biochem.2c00619.

(22) Spence, M. A.; Kaczmarski, J. A.; Saunders, J. W.; Jackson, C. J. Ancestral Sequence Reconstruction for Protein Engineers. *Curr. Opin. Struct. Biol.* **2021**, *69*, 131–141. https://doi.org/10.1016/j.sbi.2021.04.001.

(23) Starr, T. N.; Zepeda, S. K.; Walls, A. C.; Greaney, A. J.; Alkhovsky, S.; Veesler, D.; Bloom, J. D. ACE2 Binding Is an Ancestral and Evolvable Trait of Sarbecoviruses. *Nature* **2022**, *603* (7903), 913–918. https://doi.org/10.1038/s41586-022-04464-z.

(24) Meger, A. T.; Spence, M. A.; Sandhu, M.; Matthews, D.; Chen, J.; Jackson, C. J.; Raman, S. Rugged Fitness Landscapes Minimize Promiscuity in the Evolution of Transcriptional Repressors. *Cell Syst.* **2024**, *15* (4), 374-387.e6. https://doi.org/10.1016/j.cels.2024.03.002.

(25) Hartman, E. C.; Tullman-Ercek, D. Learning from Protein Fitness Landscapes: A Review of Mutability, Epistasis, and Evolution. *Curr. Opin. Syst. Biol.* **2019**, *14*, 25–31. https://doi.org/10.1016/j.coisb.2019.02.006.

(26) Livada, J.; Vargas, A. M.; Martinez, C. A.; Lewis, R. D. Ancestral Sequence Reconstruction Enhances Gene Mining Efforts for Industrial Ene Reductases by Expanding Enzyme Panels with Thermostable Catalysts. *ACS Catal.* **2023**, *13* (4), 2576–2585. https://doi.org/10.1021/acscatal.2c03859.

(27) Thomson, R. E. S.; Carrera-Pacheco, S. E.; Gillam, E. M. J. Engineering Functional Thermostable Proteins Using Ancestral Sequence Reconstruction. *J. Biol. Chem.* **2022**, *298* (10). https://doi.org/10.1016/j.jbc.2022.102435.

(28) Gumulya, Y.; Baek, J.-M.; Wun, S.-J.; Thomson, R. E. S.; Harris, K. L.; Hunter, D. J. B.; Behrendorff, J. B. Y. H.; Kulig, J.; Zheng, S.; Wu, X.; Wu, B.; Stok, J. E.; De Voss, J. J.; Schenk, G.; Jurva, U.; Andersson, S.; Isin, E. M.; Bodén, M.; Guddat, L.; Gillam, E. M. J. Engineering Highly Functional Thermostable Proteins Using Ancestral Sequence Reconstruction. *Nat. Catal.* **2018**, *1* (11), 878–888. https://doi.org/10.1038/s41929-018-0159-5.

(29) Rives, A.; Meier, J.; Sercu, T.; Goyal, S.; Lin, Z.; Liu, J.; Guo, D.; Ott, M.; Zitnick, C. L.; Ma, J.; Fergus, R. Biological Structure and Function Emerge from Scaling Unsupervised

Learning to 250 Million Protein Sequences. *Proc. Natl. Acad. Sci.* **2021**, *118* (15), e2016239118. https://doi.org/10.1073/pnas.2016239118.

(30) Lin, Z.; Akin, H.; Rao, R.; Hie, B.; Zhu, Z.; Lu, W.; Smetanin, N.; Verkuil, R.; Kabeli, O.; Shmueli, Y.; dos Santos Costa, A.; Fazel-Zarandi, M.; Sercu, T.; Candido, S.; Rives, A. Evolutionary-Scale Prediction of Atomic-Level Protein Structure with a Language Model. *Science* **2023**, *379* (6637), 1123–1130. https://doi.org/10.1126/science.ade2574.

(31) Elnaggar, A.; Heinzinger, M.; Dallago, C.; Rehawi, G.; Wang, Y.; Jones, L.; Gibbs, T.; Feher, T.; Angerer, C.; Steinegger, M.; Bhowmik, D.; Rost, B. ProtTrans: Toward Understanding the Language of Life Through Self-Supervised Learning. *IEEE Trans. Pattern Anal. Mach. Intell.* **2022**, *44* (10), 7112–7127. https://doi.org/10.1109/TPAMI.2021.3095381.

(32) Alley, E. C.; Khimulya, G.; Biswas, S.; AlQuraishi, M.; Church, G. M. Unified Rational Protein Engineering with Sequence-Based Deep Representation Learning. *Nat. Methods* **2019**, *16* (12), 1315–1322. https://doi.org/10.1038/s41592-019-0598-1.

(33) Chen, L.; Zhang, Z.; Li, Z.; Li, R.; Huo, R.; Chen, L.; Wang, D.; Luo, X.; Chen, K.; Liao, C.; Zheng, M. Learning Protein Fitness Landscapes with Deep Mutational Scanning Data from Multiple Sources. *Cell Syst.* **2023**, *14* (8), 706-721.e5. https://doi.org/10.1016/j.cels.2023.07.003.

(34) D'Costa, S.; Hinds, E. C.; Freschlin, C. R.; Song, H.; Romero, P. A. Inferring Protein Fitness Landscapes from Laboratory Evolution Experiments. *PLOS Comput. Biol.* **2023**, *19* (3), e1010956. https://doi.org/10.1371/journal.pcbi.1010956.

(35) Hie, B. L.; Yang, K. K.; Kim, P. S. Evolutionary Velocity with Protein Language Models Predicts Evolutionary Dynamics of Diverse Proteins. *Cell Syst.* **2022**, *13* (4), 274-285.e6. https://doi.org/10.1016/j.cels.2022.01.003.

(36) Matthews, D. S.; Spence, M. A.; Mater, A. C.; Nichols, J.; Pulsford, S. B.; Sandhu, M.; Kaczmarski, J. A.; Miton, C. M.; Tokuriki, N.; Jackson, C. J. Leveraging Ancestral Sequence Reconstruction for Protein Representation Learning. bioRxiv December 21, 2023, p 2023.12.20.572683. https://doi.org/10.1101/2023.12.20.572683.

(37) Joho, Y.; Vongsouthi, V.; Spence, M. A.; Ton, J.; Gomez, C.; Tan, L. L.; Kaczmarski, J. A.; Caputo, A. T.; Royan, S.; Jackson, C. J.; Ardevol, A. Ancestral Sequence Reconstruction Identifies Structural Changes Underlying the Evolution of Ideonella Sakaiensis PETase and Variants with Improved Stability and Activity. *Biochemistry* **2023**, *62* (2), 437–450. https://doi.org/10.1021/acs.biochem.2c00323.

(38) Hoang, D. T.; Chernomor, O.; von Haeseler, A.; Minh, B. Q.; Vinh, L. S. UFBoot2: Improving the Ultrafast Bootstrap Approximation. *Mol. Biol. Evol.* **2018**, *35* (2), 518–522. https://doi.org/10.1093/molbev/msx281.

(39) Yang, Z. PAML 4: Phylogenetic Analysis by Maximum Likelihood. *Mol. Biol. Evol.* **2007**, *24* (8), 1586–1591. https://doi.org/10.1093/molbev/msm088.

(40) Eick, G. N.; Bridgham, J. T.; Anderson, D. P.; Harms, M. J.; Thornton, J. W. Robustness of Reconstructed Ancestral Protein Functions to Statistical Uncertainty. *Mol. Biol. Evol.* **2017**, *34* (2), 247–261. https://doi.org/10.1093/molbev/msw223.

(41) Shimodaira, H. An Approximately Unbiased Test of Phylogenetic Tree Selection. *Syst. Biol.* **2002**, *51* (3), 492–508. https://doi.org/10.1080/10635150290069913.

(42) Han, X.; Liu, W.; Huang, J.-W.; Ma, J.; Zheng, Y.; Ko, T.-P.; Xu, L.; Cheng, Y.-S.; Chen, C.-C.; Guo, R.-T. Structural Insight into Catalytic Mechanism of PET Hydrolase. *Nat. Commun.* **2017**, *8* (1), 2106. https://doi.org/10.1038/s41467-017-02255-z.

(43) Guo, B.; Vanga, S. R.; Lopez-Lorenzo, X.; Saenz-Mendez, P.; Ericsson, S. R.; Fang, Y.; Ye, X.; Schriever, K.; Bäckström, E.; Biundo, A.; Zubarev, R. A.; Furó, I.; Hakkarainen, M.; Syrén, P.-O. Conformational Selection in Biocatalytic Plastic Degradation by PETase. *ACS Catal.* **2022**, *12* (6), 3397–3409. https://doi.org/10.1021/acscatal.1c05548.

(44) Crnjar, A.; Griñen, A.; Kamerlin, S. C. L.; Ramírez-Sarmiento, C. A. Conformational Selection of a Tryptophan Side Chain Drives the Generalized Increase in Activity of PET Hydrolases through a Ser/Ile Double Mutation. *ACS Org. Inorg. Au* **2023**, *3* (2), 109–119. https://doi.org/10.1021/acsorginorgau.2c00054.

(45) Varadi, M.; Anyango, S.; Deshpande, M.; Nair, S.; Natassia, C.; Yordanova, G.; Yuan, D.; Stroe, O.; Wood, G.; Laydon, A.; Žídek, A.; Green, T.; Tunyasuvunakool, K.; Petersen, S.; Jumper, J.; Clancy, E.; Green, R.; Vora, A.; Lutfi, M.; Figurnov, M.; Cowie, A.; Hobbs, N.; Kohli, P.; Kleywegt, G.; Birney, E.; Hassabis, D.; Velankar, S. AlphaFold Protein Structure Database: Massively Expanding the Structural Coverage of Protein-Sequence Space with High-Accuracy Models. *Nucleic Acids Res.* **2022**, *50* (D1), D439–D444. https://doi.org/10.1093/nar/gkab1061.

(46) Jumper, J.; Evans, R.; Pritzel, A.; Green, T.; Figurnov, M.; Ronneberger, O.; Tunyasuvunakool, K.; Bates, R.; Žídek, A.; Potapenko, A.; Bridgland, A.; Meyer, C.; Kohl, S. A. A.; Ballard, A. J.; Cowie, A.; Romera-Paredes, B.; Nikolov, S.; Jain, R.; Adler, J.; Back, T.; Petersen, S.; Reiman, D.; Clancy, E.; Zielinski, M.; Steinegger, M.; Pacholska, M.; Berghammer, T.; Bodenstein, S.; Silver, D.; Vinyals, O.; Senior, A. W.; Kavukcuoglu, K.; Kohli, P.; Hassabis, D. Highly Accurate Protein Structure Prediction with AlphaFold. *Nature* **2021**, *596* (7873), 583–589. https://doi.org/10.1038/s41586-021-03819-2.

(47) Liu, Y.; Eisenberg, D. 3D Domain Swapping: As Domains Continue to Swap. *Protein Sci. Publ. Protein Soc.* **2002**, *11* (6), 1285–1299.

(48) Then, J.; Wei, R.; Oeser, T.; Barth, M.; Belisário-Ferrari, M. R.; Schmidt, J.; Zimmermann, W. Ca2+ and Mg2+ Binding Site Engineering Increases the Degradation of Polyethylene

Terephthalate Films by Polyester Hydrolases from Thermobifida Fusca. *Biotechnol. J.* **2015**, *10* (4), 592–598. https://doi.org/10.1002/biot.201400620.

(49) Then, J.; Wei, R.; Oeser, T.; Gerdts, A.; Schmidt, J.; Barth, M.; Zimmermann, W. A Disulfide Bridge in the Calcium Binding Site of a Polyester Hydrolase Increases Its Thermal Stability and Activity against Polyethylene Terephthalate. *FEBS Open Bio* **2016**, *6* (5), 425–432. https://doi.org/10.1002/2211-5463.12053.

(50) Joho, Y.; Vongsouthi, V.; Spence, M. A.; Ton, J.; Gomez, C.; Tan, L. L.; Kaczmarski, J. A.; Caputo, A. T.; Royan, S.; Jackson, C. J.; Ardevol, A. Ancestral Sequence Reconstruction Identifies Structural Changes Underlying the Evolution of Ideonella Sakaiensis PETase and Variants with Improved Stability and Activity. *Biochemistry* **2023**, *62* (2), 437–450. https://doi.org/10.1021/acs.biochem.2c00323.

(51) Daković, M.; Stanković, L.; Sejdić, E. Local Smoothness of Graph Signals. *Math. Probl. Eng.* **2019**, *2019*, e3208569. https://doi.org/10.1155/2019/3208569.

(52) Castro, E.; Godavarthi, A.; Rubinfien, J.; Givechian, K.; Bhaskar, D.; Krishnaswamy, S. Transformer-Based Protein Generation with Regularized Latent Space Optimization. *Nat. Mach. Intell.* **2022**, *4* (10), 840–851. https://doi.org/10.1038/s42256-022-00532-1.

(53) Fu, L.; Niu, B.; Zhu, Z.; Wu, S.; Li, W. CD-HIT: Accelerated for Clustering the next-Generation Sequencing Data. *Bioinformatics* **2012**, *28* (23), 3150–3152. https://doi.org/10.1093/bioinformatics/bts565.

(54) Petersen, T. N.; Brunak, S.; von Heijne, G.; Nielsen, H. SignalP 4.0: Discriminating Signal Peptides from Transmembrane Regions. *Nat. Methods* **2011**, *8* (10), 785–786. https://doi.org/10.1038/nmeth.1701.

(55) Katoh, K.; Standley, D. M. MAFFT Multiple Sequence Alignment Software Version 7: Improvements in Performance and Usability. *Mol. Biol. Evol.* **2013**, *30* (4), 772–780. https://doi.org/10.1093/molbev/mst010.

(56) Minh, B. Q.; Schmidt, H. A.; Chernomor, O.; Schrempf, D.; Woodhams, M. D.; von Haeseler, A.; Lanfear, R. IQ-TREE 2: New Models and Efficient Methods for Phylogenetic Inference in the Genomic Era. *Mol. Biol. Evol.* **2020**, *37* (5), 1530–1534. https://doi.org/10.1093/molbev/msaa015.

(57) Kalyaanamoorthy, S.; Minh, B. Q.; Wong, T. K. F.; von Haeseler, A.; Jermiin, L. S. ModelFinder: Fast Model Selection for Accurate Phylogenetic Estimates. *Nat. Methods* **2017**, *14* (6), 587–589. https://doi.org/10.1038/nmeth.4285.

(58) Le, S. Q.; Gascuel, O. An Improved General Amino Acid Replacement Matrix. *Mol. Biol. Evol.* **2008**, *25* (7), 1307–1320. https://doi.org/10.1093/molbev/msn067.

(59) Gibson, D. G.; Young, L.; Chuang, R.-Y.; Venter, J. C.; Hutchison, C. A.; Smith, H. O. Enzymatic Assembly of DNA Molecules up to Several Hundred Kilobases. *Nat. Methods* **2009**, *6* (5), 343–345. https://doi.org/10.1038/nmeth.1318.

(60) Studier, F. W. Stable Expression Clones and Auto-Induction for Protein Production in E. Coli. *Methods Mol. Biol. Clifton NJ* **2014**, *1091*, 17–32. https://doi.org/10.1007/978-1-62703-691-7_2.

(61) Aragão, D.; Aishima, J.; Cherukuvada, H.; Clarken, R.; Clift, M.; Cowieson, N. P.; Ericsson, D. J.; Gee, C. L.; Macedo, S.; Mudie, N.; Panjikar, S.; Price, J. R.; Riboldi-Tunnicliffe, A.; Rostan, R.; Williamson, R.; Caradoc-Davies, T. T. MX2: A High-Flux Undulator Microfocus Beamline Serving Both the Chemical and Macromolecular Crystallography Communities at the Australian Synchrotron. *J. Synchrotron Radiat.* **2018**, *25* (Pt 3), 885–891. https://doi.org/10.1107/S1600577518003120.

(62) Kabsch, W. XDS. *Acta Crystallogr. D Biol. Crystallogr.* **2010**, *66* (2), 125–132. https://doi.org/10.1107/S0907444909047337.

(63) Winn, M. D.; Ballard, C. C.; Cowtan, K. D.; Dodson, E. J.; Emsley, P.; Evans, P. R.; Keegan, R. M.; Krissinel, E. B.; Leslie, A. G. W.; McCoy, A.; McNicholas, S. J.; Murshudov, G. N.; Pannu, N. S.; Potterton, E. A.; Powell, H. R.; Read, R. J.; Vagin, A.; Wilson, K. S. Overview of the CCP4 Suite and Current Developments. *Acta Crystallogr. D Biol. Crystallogr.* **2011**, *67* (Pt 4), 235–242. https://doi.org/10.1107/S0907444910045749.

(64) Adams, P. D.; Afonine, P. V.; Bunkóczi, G.; Chen, V. B.; Davis, I. W.; Echols, N.; Headd, J. J.; Hung, L.-W.; Kapral, G. J.; Grosse-Kunstleve, R. W.; McCoy, A. J.; Moriarty, N. W.; Oeffner, R.; Read, R. J.; Richardson, D. C.; Richardson, J. S.; Terwilliger, T. C.; Zwart, P. H. PHENIX: A Comprehensive Python-Based System for Macromolecular Structure Solution. *Acta Crystallogr. D Biol. Crystallogr.* **2010**, *66* (Pt 2), 213–221. https://doi.org/10.1107/S0907444909052925.

(65) Emsley, P.; Cowtan, K. Coot: Model-Building Tools for Molecular Graphics. *Acta Crystallogr. D Biol. Crystallogr.* **2004**, *60* (Pt 12 Pt 1), 2126–2132. https://doi.org/10.1107/S0907444904019158.

(66) Castro, E.; Benz, A.; Tong, A.; Wolf, G.; Krishnaswamy, S. Uncovering the Folding Landscape of RNA Secondary Structure with Deep Graph Embeddings. arXiv March 28, 2022. https://doi.org/10.48550/arXiv.2006.06885.